energy&fuels

pubs.acs.org/EF
Article

Heat Loss Effects on Emissions in an NH_3 RRQL Combustor

Published as part of Energy & Fuels special issue "Recent Advances in Ammonia Energy: Top Research from the 4th SoAE".

Renee Cole,* Ananth S. Nayak, Cristian Avila, David R. Noble, David Wu, Benjamin Emerson, and Timothy Lieuwen

Cite This: *Energy Fuels* 2026, 40, 12098−12108

ABSTRACT: Ammonia (NH_3) is a carbon-free energy carrier with an infrastructure for production, storage, and distribution. There is interest in direct NH_3 combustion, but managing pollutant emissions is a key challenge, particularly nitric oxides (NO_x) due to the fuel-bound nitrogen atom, nitrous oxide (N_2O), which is a potent greenhouse gas, and unburned NH_3, which is harmful to humans and the environment. Rich staged combustor concepts with extended primary residence times ($\tau_{res,primary}$), like Rich-Relax-Quick-mix-Lean (RRQL), offer a viable pathway for direct NH_3 combustion with low levels of NO_x formation. However, minimizing secondary emissions such as N_2O and unburned NH_3 and hydrogen (H_2) remains a critical challenge. Prior atmospheric-pressure studies have demonstrated that RRQL operation with sufficiently long $\tau_{res,primary}$ enables substantial NO_x relaxation and promotes NH_3 cracking to H_2, if heat losses from the relaxation stage are limited. However, the combined influence of elevated pressure and long residence time on RRQL performance has not been explored. The present work examines RRQL operation at pressures up to 5 bar and elevated $\tau_{res,primary}$. Exhaust measurements of NO_x, NH_3, and N_2O are used to quantify the extent of NO_x relaxation and NH_3 cracking under nonadiabatic conditions. To contextualize and quantify the effects of heat losses in the experimental data, chemical reactor networks (CRNs) incorporating prescribed heat loss rates are employed to assess the sensitivity of emissions to thermal losses in the relaxation stage. Collectively, the results demonstrate that management and quantification of heat losses are essential to preserve NO_x relaxation and limit NH_3 and N_2O emissions.

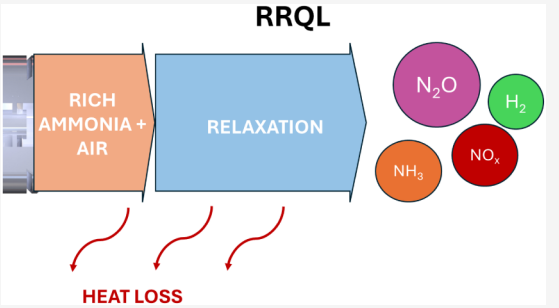

INTRODUCTION

Ammonia (NH_3) and hydrogen (H_2) are being explored as potential energy carriers for a decarbonized energy and industrial sector. NH_3, in particular, has a high energy density, established infrastructure for production, storage, distribution, and ease of liquefaction, which makes it particularly promising compared to H_2.[1,2] Direct combustion of NH_3 presents significant challenges, including a high ignition temperature, low flame speed,[3,4] and complex kinetics,[5,6] which contribute to poor reactivity and stability in conventional combustor architectures.[7] Furthermore, NH_3 contains fuel-bound nitrogen, which can produce large quantities of nitric oxide (NO_x) and nitrous oxide (N_2O). Unburned NH_3 and H_2 are also products of inefficient NH_3 combustion, which can be particularly harmful.[8] Furthermore, it is important to recognize that lean, premixed strategies designed to minimize NO_x formation from atmospheric nitrogen in air are effective for the combustion of hydrocarbons and H_2 but are not effective for managing NO_x emissions from NH_3.[1,9−11] Thus, while NH_3 is carbon-free, it is not inherently clean without careful mitigation steps and advanced combustion strategies. Among these, staged architectures such as Rich-Quench-Lean (RQL) and Rich-Relax-Quick-mix-Lean (RRQL) have shown potential to suppress NO_x formation. The RQL strategy fundamentally leverages the fuel-rich chemistry in the primary zone, with lean secondary combustion, to ensure combustion efficiency and prevent fuel slip.[10,12−14]

The RRQL combustor, presented by Cole et al.[15] and Avila et al.,[16] differs from the traditional RQL strategy by significantly extending the primary stage residence time ($\tau_{res,primary}$) to allow NO_x relaxation toward equilibrium values, which are very low for rich NH_3 combustion.[17,18] The relaxation stage enables nonoxidative cracking of NH_3 into H_2, thereby reducing NH_3 levels and potential fuel-bound NO_x production in the secondary stage. Moreover, elevated chamber pressures (P_0) both decrease equilibrium NO_x emissions and accelerate NO_x

Received: January 31, 2026
Revised: April 27, 2026
Accepted: May 6, 2026
Published: May 25, 2026

https://doi.org/10.1021/acs.energyfuels.6c00593
Energy Fuels 2026, 40, 12098−12108

relaxation toward equilibrium.[19] The RRQL combustor has well-understood operating parameters for flame stability and emissions under atmospheric conditions. These results also show that the elevated $\tau_{res,primary}$ required to realize NO_x relaxation at atmospheric conditions (~100 ms) can lead to high heat losses. These heat losses can significantly slow, or even freeze, NO_x relaxation and NH_3 cracking while promoting N_2O production; therefore, they should be carefully considered.

Recent studies also show that emission species such as NH_3, N_2O, NO_x, and H_2 are sensitive to wall heat losses for NH_3-air flames,[20−22] and that RRQL combustor N_2O and NH_3 emissions can be orders of magnitude greater than those predicted by adiabatic computations.[15,16] Furthermore, the effects of elevated P_0 with heat losses have been experimentally shown to increase NO_x emissions and to exhibit other trends not predicted by adiabatic models.[21] Wall heat losses, which may be particularly high in small-diameter lab-scale combustors, quartz combustor liners used for optical access, or elevated residence time combustors, can cause emissions to vary by orders of magnitude.[23] In these staged combustion systems, both lowering wall heat losses and extending the $\tau_{res,primary}$ are effective in reducing overall emissions, and increasing $\tau_{res,primary}$ enhances NO_x relaxation and promotes NH_3 cracking, producing emission trends comparable to those achieved through improved thermal insulation. Consistent with this behavior, Avila et al.[24] reported that mitigating wall heat losses suppresses unburned NH_3 slip from the primary stage and leads to lower N_2O emissions under staged operating conditions.

In this article, results from an RRQL combustor are presented at pressures up to 5 bar, providing new experimental insight into NH_3-air combustion at elevated primary stage residence times and inlet pressures. Complementary kinetic simulations examine the role of heat losses in shaping emissions and reconcile discrepancies between prior adiabatic predictions and experimental observations. Together, these results advance the assessment of RRQL feasibility and offer guidance for low-emission NH_3 combustors under gas turbine-relevant operating conditions.

METHODS

Burner and Conditions

Experiments are performed using a laboratory-scale swirl-stabilized burner illustrated in Figure 1. The burner incorporates an axial swirler with a geometric swirl number (S_g) of 1.1, consisting of 16 flat vanes.[15] All tests are conducted at a fixed nozzle bulk velocity (U_0) of 1.0 m/s. Primary and secondary air mass flow rates are independently metered using MC-series laminar differential pressure mass flow controllers (Alicat Scientific), which provide an accuracy of ±0.8% of the measured value. Fuel delivery is controlled via a critical orifice, with the mass flow rate inferred from the pressure drop across the orifice and regulated using an electronic pressure controller. Sonic flow conditions are verified using an upstream pressure transducer and thermocouple, along with a downstream pressure measurement to ensure accurate fuel metering, with an accuracy of ±3%. Collectively, the air and fuel control systems maintain both the primary ($\phi_{primary}$) and global (ϕ_{global}) equivalence ratios within ±3% uncertainty. The burner assembly is mounted inside a pressure vessel equipped with optically accessible windows. There are three air injection circuits: primary, secondary, and shroud air. The primary, secondary, and shroud air circuits are supplied with cold air at 300 K. The shroud air circuit serves to pressurize the vessel, with higher flow rates required to achieve higher pressures due to the fixed exhaust choke. Therefore, enhanced heat losses occur at elevated pressures in the present experimental configuration. A pressure transducer monitors the pressure inside the vessel. Various

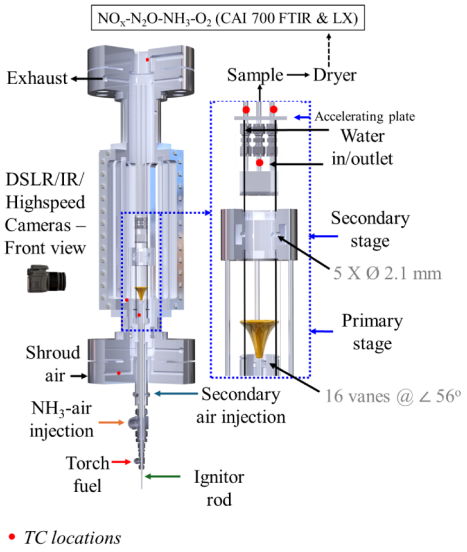

Figure 1. Experimental setup.

thermocouples monitor the shroud, exhaust emissions, and exhaust temperatures.

The primary stage of the combustor is a cylindrical quartz tube with an inner diameter of 52 mm and a wall thickness of 4 mm. The length of the primary stage is 178 mm to allow for NO_x relaxation on the order of 10^2 ppm (parts per million), according to Gubbi et al.[17] The secondary air is inserted through one row of five holes of diameter 2.1 mm at the end of the primary stage to allow for high jet momentum ratios (J) and promote mixing in the secondary stage.[16] Note that the J values are approximately equivalent for each unique ϕ_{global} with less than 10% variation due to changes in crossflow density and $\phi_{primary}$, and the values in Table 1 correspond to $\phi_{primary}$ of 1.13. A block plate is installed 150 mm downstream from the secondary air injection to accelerate the flow and prevent interaction with the shroud air. Additional details of the burner design and facility are provided in Cole et al.[15,25] and Avila et al.[16,24,]

Table 1. Experimental Test Matrix

Parameter	Value
Primary equivalence ratio ($\phi_{primary}$)	1.08/1.13/1.18
Global equivalence ratio (ϕ_{global})	$\phi_{primary}$/0.9/0.50
Jet momentum ratio (J)	0/70/1800
Nozzle velocity (U_0)	1 m/s
Geometric swirl (S_g)	1.1
Inlet temperature (T_0)	300 K
Inlet shroud temperature (T_s)	300 K
Inlet pressure (P_0)	1/3/5 bar
Thermal power (Q) ($\phi_{primary}$ = 1.13)	0.7/2.3/3.2 kW
Ammonia mol fraction (X_{NH_3})	1.0

Exhaust Emissions

Gas-phase exhaust emissions are quantified using a California Analytical Instruments 700 LX NDIR/O_2 analyzer for O_2 and CO measurements, in conjunction with a 700 FTIR analyzer capable of detecting NO_x, NH_3, and N_2O. A water-cooled, area-weighted rake probe was positioned at an axial distance of 300 mm downstream of the dump plane, corresponding to a nominal $\tau_{res,primary}$ of approximately 250 ms relative to the visible flame brush. Detailed information on the rake probe geometry and sampling methodology is provided in Cole et al.[25] Thermocouples integrated into the probe monitor the sample gas temperature and the inlet and outlet water temperatures, ensuring rapid quenching of the exhaust stream and effective freezing of NO_x chemistry. The probe temperature is maintained at 400−450 K to

https://doi.org/10.1021/acs.energyfuels.6c00593
Energy Fuels 2026, 40, 12098−12108

ensure the sample is quenched and the NO_x chemistry is frozen. Following extraction, the sample is dried to remove excess moisture and transported through a heated line maintained at 190 °C prior to analysis. A calibration study through the sampling system indicates that passage through the condenser resulted in an apparent reduction of ~150 ppm of NH_3, due to its water solubility, which should be noted when interpreting absolute NH_3 levels. Other emissions, including N_2O, NO_x, and O_2, are not affected by this process. All reported exhaust concentrations are corrected to a dry basis at 15% O_2,[26] and correspond to the operating conditions summarized in Table 1.

Chemical Reactor Network

Reduced-order modeling using a chemical reactor network (CRN) is applied to the rich and relaxation stages of the RRQL NH_3 combustor architecture, as shown in Figure 2. The reactor network used for comparison with experimental results is similar to approaches used in other literature sources.[18,23] The rich primary stage is represented as a perfectly stirred reactor (PSR) with a residence time of 1 ms. The relaxation stage is represented as a plug flow reactor (PFR) with a residence time of 250 ms; the combination of both is comparable to $\tau_{res,primary}$ in the experimental RRQL combustor described in the previous section. The PSR is fed with premixed NH_3-air mixtures, with corresponding mass flow rates and thermal powers, which scale with P_0, as the experiments are run at a constant U_0. The PSR is run under adiabatic conditions because residence times are 2 orders of magnitude lower, whereas the PFR incorporates heat losses. This PSR−PFR representation was selected to reflect the dominant transport characteristics of the two combustor regions in a reduced-order model. The rich primary stage is swirl-stabilized and dominated by strong recirculation and rapid mixing, making a PSR approximation appropriate for the short residence time flame zone. In contrast, the downstream relaxation stage is intended to capture postflame axial evolution over an extended residence time, during which temperature and composition change progressively as NO_x relaxation and nonoxidative NH_3 cracking proceed. For this reason, the relaxation stage is represented as a PFR.

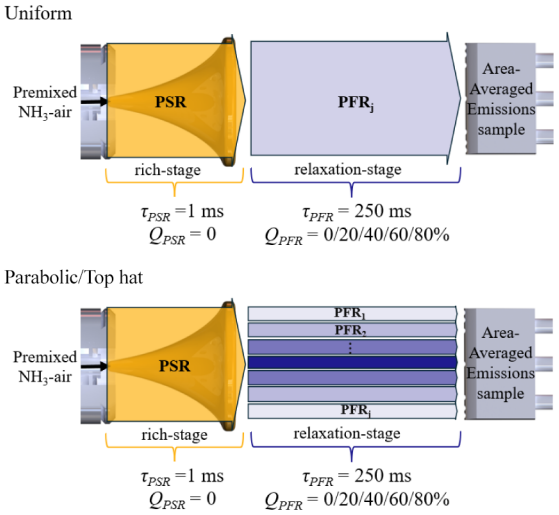

Figure 2. Chemical reactor networks with radially uniform (top) and variable (bottom) heat losses in the relaxation stage.

Heat transfer coefficients were specified from an adiabatic case up to 80% of the primary stage thermal power (Q) to quantify the impact of heat loss on emissions. While the upper bound of 80% heat loss represents an extreme condition approaching quenching limits, it is included to capture limiting behavior and establish sensitivity bounds for the relaxation stage chemistry. Importantly, experimental measurements indicate that substantial heat losses occur in the present combustor. Based on traversing thermocouple measurements along the combustor centerline, heat losses of approximately ~45% are estimated over the 130 mm relaxation stage at 1 bar.[15] These elevated losses are attributed to the high surface area-to-volume ratio and enhanced convective cooling in the laboratory-scale configuration, particularly under elevated pressure, where shroud flow increases. Therefore, the selected heat loss range spans both experimentally relevant conditions and upper-bound cases needed to interpret emission sensitivity.

It is also recognized that heat losses are distributed radially and that this radial distribution can materially impact emission trends. For example, previous emissions data from this combustor at 1 bar, obtained with a single-point probe at various radial and axial positions, show that at 80 ms from the flame brush, NH_3 emissions may increase by 30−300% from the centerline to the wall. At the same time, NO_x and N_2O both vary by less than 15%.[15] Therefore, for the PFR, three different models for radial heat losses were deployed, with each distributing heat losses in different ways over an array of PFRs, as shown in Figure 2, where each PFR_j represents a radial subregion of the liner. These models include a uniform, parabolic, and top-hat model, which are detailed in the following section.

In the uniform heat loss case, shown in eq 1.a, all radial locations are assigned the same heat loss rate, such that the relaxation stage may be modeled using a single PFR without radial resolution. The parabolic radial distribution of heat losses is prescribed as a fraction of the thermal power using a normalized parabolic profile in eq 1.a, where $\eta = r/R$ is the nondimensional radial coordinate, r is the radial position, R is the combustor liner inner radius, and a (equivalent to 3 for the following study) is a shape parameter controlling the degree of wall-peaked heat loss. The selected value of a produces a moderately wall biased heat loss profile that avoids unrealistically extreme near wall localization. The normalization ensures that the area-weighted average of $w(\eta)$ over the cross-section is unity. In addition to the parabolic profile, an alternative tophat distribution is also examined, in which the liner cross-section is divided into a core region and a near wall annulus. The heat loss weighting function is defined in eq 1.a, where $\eta_c = \frac{R-\delta}{R} = 0.85$ defines the thickness δ of the near wall annulus, and b (equivalent to 3 for the following study) imposes an approximately 3-fold enhancement in wall

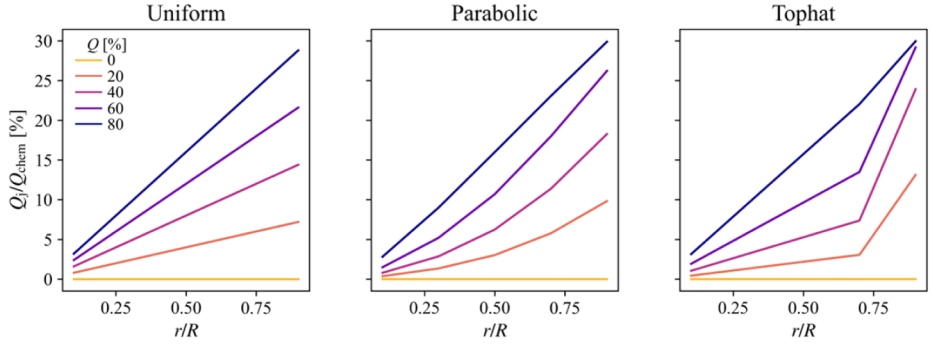

Figure 3. Uniform, parabolic, and tophat profiles of radial distributions of heat loss calculated relative to the chemical energy of the primary stage.

https://doi.org/10.1021/acs.energyfuels.6c00593
Energy Fuels 2026, 40, 12098−12108

region heat losses, representing a physically reasonable upper bound that avoids unrealistically extreme near wall localization.

Uniform

$$w(\eta) = 1 \tag{1.a}$$

Parabolic

$$w(\eta) = \frac{1 + a\eta^2}{1 + \frac{a}{2}} \tag{1.b}$$

Tophat

$$w(\eta) = \begin{cases} \dfrac{1}{1 + b(1 - \eta_c^2)}, & 0 \le \eta < \eta_c \\ \dfrac{1 + b}{1 + b(1 - \eta_c^2)}, & \eta_c \le \eta \le 1 \end{cases} \tag{1.c}$$

Each base PSR_j, representing a radial subregion of the liner, is assigned a heat loss fraction as shown in eq 1.b, where Q_{PFR} is the prescribed area-weighted average heat loss, expressed as a fraction of the thermal power, and η_j denotes the representative radial location of the subregion. The profile is normalized so that the area-weighted mean heat loss remains equivalent to the 0−80% heat losses prescribed to the uniform PSR, to assess the sensitivity of the relaxation stage chemistry to both the magnitude and radial distribution of heat losses. The resulting profiles for the uniform, parabolic, and tophat are illustrated in Figure 3. As the plotted per-bin loss is an extensive quantity, the annular area in a bin is proportional to the bin's radial location, thereby weighting the distribution toward outer bins, making the normalized parabolic and tophat profiles appear similar at high Q.

$$Q_{PFR,j} = Q_{PFR} w(\eta_j) \tag{2}$$

For cases employing radial discretization, such as the parabolic and tophat, the outlet emissions and thermochemical quantities from the relaxation stage are reconstructed by recombining the individual radial subregions using an area-weighted average, as given by eq 1.c As discrete CRN represents an annular region of the liner with cross-sectional area A_j. The area-weighted recombination yields a single, cross-section-averaged outlet state, $\bar{\psi}$, for reporting emissions and temperatures. Under the assumption of uniform axial velocity, this area-weighted averaging is equivalent to a mass-flow-weighted average and preserves the prescribed mean heat loss fraction.

$$\bar{\psi} = \sum_{j=1}^{N_b} \left(\frac{A_j}{A_{total}} \right) \psi_j \tag{3}$$

Simulations are conducted using the Stagni et al.,[27] Mei et al.,[28] and Zhang et al.[29] kinetic mechanisms, which were selected based on their reported ability to reasonably reproduce laminar burning velocities and speciation data for NH_3-based flames at elevated P_0. The results section focuses on the Stagni mechanism; the Mei and Zhang mechanisms are detailed in the Supporting Information.

RESULTS

Flame Imaging

Figure 4 illustrates 0.5 s time-averaged images of the primary stage flame, recorded with a DSLR camera (f/16, 800 ISO) for sweeps of P_0 and $\phi_{primary}$, as summarized in Table 1. In general, the primary flame presents typical shear-stabilized morphologies for swirling flames.[30] At lower and higher pressures, the primary stage flame is stabilized in the inner shear layer and both the inner and outer shear layers, respectively. With outer shear layer stabilization, the flame clearly interacts with the outer recirculation zone (ORZ) as well. With increasing $\phi_{primary}$ the flame height and visible luminosity increase. Furthermore, increasing P_0 causes a marginal decrease in flame height, an

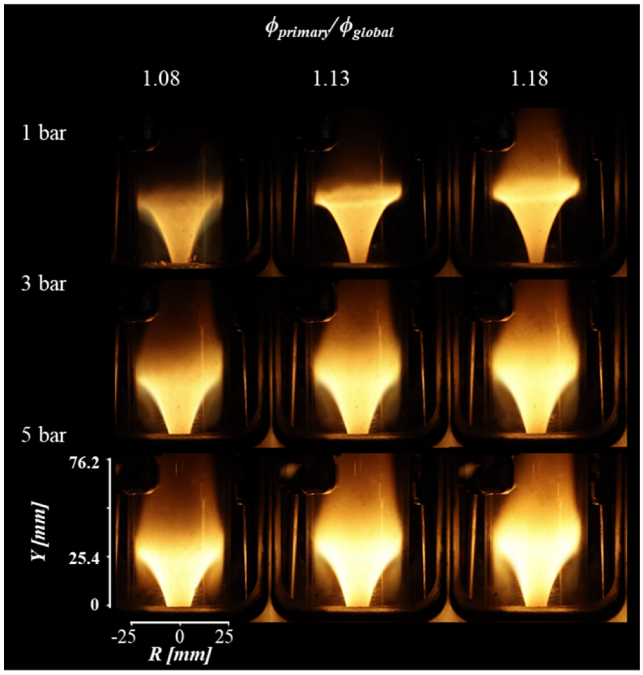

Figure 4. DSLR images of the primary stage flame.

increase in flame base width, and an increase in visible luminosity. These findings were also confirmed by Khateeb et al.[7] The increasing luminosity is expected due to the increase in thermal power with P_0 at a constant U_0. Overall, the visible flame images show a stable, compact flame for the test matrix in Table 1, confirming the operability of the combustor's rich stage at elevated P_0.

Experimental Emissions

Figures 5 and 6 show the influence of $\phi_{primary}$ and ϕ_{global} on NO_x and NH_3/N_2O emissions, respectively, for various P_0 at a $\tau_{res,primary}$ of 250 ms

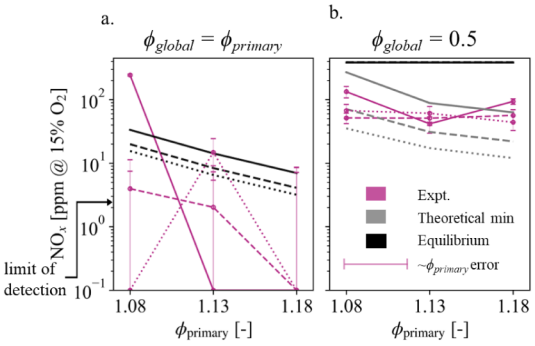

Figure 5. Experimental emissions data for various P_0 at a $\tau_{res,primary}$ of 250 ms, overlaid with theoretical minima and equilibrium NO_x data. Note that the $\phi_{primary}$ uncertainty is represented in an error bar in the legend for clarity. Figure 5.a shows emission trends for the primary stage ($\phi_{global} = \phi_{primary}$), where emissions are measured after the rich stage. Figure 5.b shows $\phi_{global} = 0.5$, indicating overall staged results in which the primary stage is operated fuel-rich and the combustor is overall operated fuel-lean.

from the flame brush. It should be noted that as P_0 increases, the shroud mass flow rate increases proportionally, leading to greater convective heat losses. In addition to the experimental data, Figure 5 also shows the theoretical minimum NO_x for the staged case ($\phi_{global} = 0.5$), calculated as prescribed by Gubbi et al.,[19] as well as equilibrium NO_x emissions for

https://doi.org/10.1021/acs.energyfuels.6c00593
Energy Fuels 2026, 40, 12098−12108

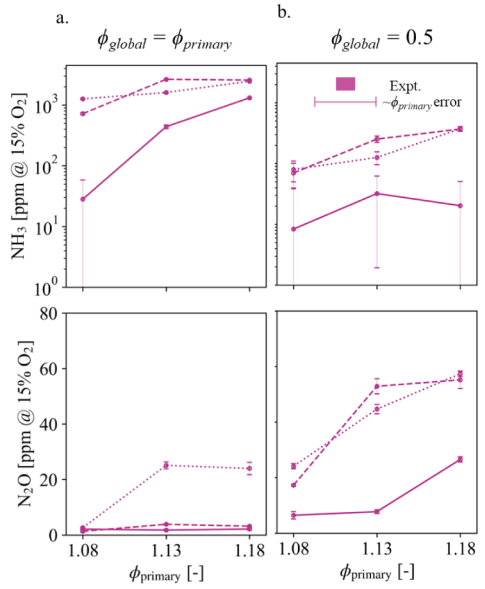

Figure 6. Experimental emissions data for various P_0 at a $\tau_{res,primary}$ of 250 ms. Note that the $\phi_{primary}$ uncertainty is represented by an error bar in the legend for clarity. Figure 6.a shows emission trends for the primary stage ($\phi_{global} = \phi_{primary}$), where emissions are measured after the rich stage. Figure 6.b, where $\phi_{global} = 0.5$, indicates overall staged results in which the primary stage is operated fuel-rich and the combustor is overall operated fuel-lean.

both the nonstaged ($\phi_{global} = \phi_{primary}$) and staged case (calculated at $\phi_{global} = 0.5$).

The nonstaged ($\phi_{global} = \phi_{primary}$) NO_x emissions are very close to their equilibrium counterparts at $\phi_{primary}$ values of 1.13 and 1.18, especially when accounting for experimental uncertainty, whereas $\phi_{primary}$ of 1.08 exceeds the equilibrium value significantly. However, many measurements are at the lower end of instrument detectability, leading to particularly high uncertainties. For example, the 3-bar NO_x emissions, which are near the limit of detection, are sub-20 ppm (15% dry O_2), which is of the same order of magnitude as their equilibrium values of 5−20 ppm (15% dry O_2), and the 5-bar data is sub-4 ppm (15% dry O_2), while the equilibrium values are 3−15 ppm (15% dry O_2). There is a clear monotonic trend: increasing P_0 leads to decreasing NO_x emissions in the nonstaged case, as expected from prior studies.[17] However, there are diminishing returns at P_0 above 3 bar, which may be attributed to combustion inefficiencies associated with increased heat losses due to the coupled relationship among P_0, shroud air flow rate, and convective heat losses, leading to very low levels of NO_x production.

With staged secondary air, NO_x production increases significantly, and the NO_x emissions are similar to their theoretical minimum counterparts. Furthermore, NO_x emissions and theoretical minimums are much lower than staged equilibrium emissions, highlighting the benefits of the RRQL architecture.

The nonstaged ($\phi_{global} = \phi_{primary}$) NH_3 emissions show increasing NH_3 slip with $\phi_{primary}$, as expected for rich NH_3 flames. However, they are all orders of magnitude greater than their parts-per-billion adiabatic equilibrium counterparts, reflecting heat loss effects. As P_0 increases, NH_3 slip increases by up to 140%, potentially due to heat losses, as discussed further in the following sections and compared with more detailed CRNs. The staged NH_3 emissions, however, indicate that the majority of NH_3 leaving the primary stage is ultimately consumed in the secondary stage, where this NH_3 slip contributes to the total NO_x emissions, up to 98% of which are produced in the secondary stage. In contrast, and similar to the NO_x emissions, N_2O production also increases substantially from the nonstaged to the staged case, accounting for 20−40% of the combined NO_x−N_2O emissions. As hypothesized by Okafor et al.,[21] this is a potential outcome for combustors with high heat losses, where N_2O emissions are significantly greater than their parts-per-billion equilibrium counterparts.

Figure 7 replots this data and displays NO_x and N_2O emissions as a function of NH_3 for an expanded set of ϕ_{global}, which are traced with

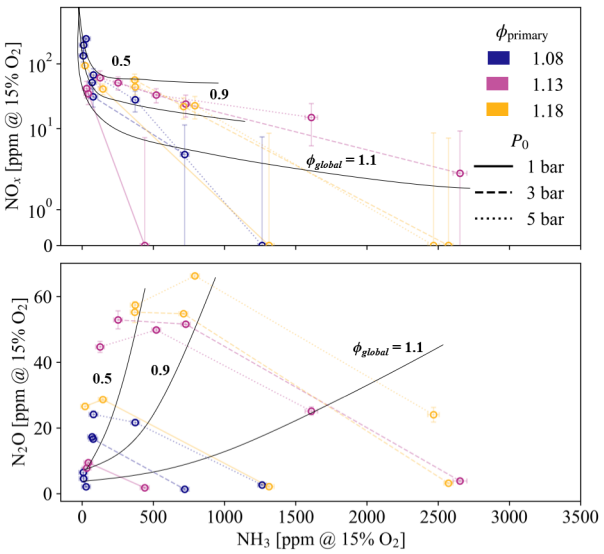

Figure 7. NO_x and N_2O emissions as a function of NH_3 with isocontours denoting ϕ_{global}.

isocontours. Generally, as the NH_3 concentration decreases, N_2O and NO_x emissions increase, as expected with decreasing ϕ_{global}, consistent with a general nitrogen balance. Generally, NO_x emissions increase dramatically with ϕ_{global}, and they are less sensitive to both pressure and $\phi_{primary}$. In contrast, the N_2O emissions are highly affected by pressure, particularly for nonoptimal $\phi_{primary}$ that allow >1500 ppm (15% dry O_2) of NH_3 slip, for the nonstaged ($\phi_{primary} = \phi_{global}$) or rich ϕ_{global}. Pressure is strongly linked to increased heat losses in this experimental setup, indicating that with elevated heat losses, the nitrogen released from NH_3 in the secondary stage is likely to form N_2O emissions, which have particularly high global-warming potential and should be minimized.[31] Furthermore, in lean ϕ_{global} cases, N_2O production also increases rapidly due to a stronger cooling effect from the cold secondary air injection.

Figure 8 reframes these trends as a nitrogen atom budget and quantifies how nitrogen introduced as NH_3 in the primary stage is distributed among the measured exhaust species. Emissions are expressed as a percentage of the fuel-bound nitrogen inventory, and the nitrogen budget plots are structured such that each bar represents the distribution of fuel-bound nitrogen among NH_3, NO_x, and N_2O with the remaining balance attributed to N_2. For example, at $\phi_{primary}$ of 1.08, ϕ_{global} of 0.5, and 5 bar, measured concentrations of NH_3, NO_x, and N_2O are 0.055%, 0.045%, and 0.035%, respectively, while the remaining N_2 is assumed to be 99.865% of the original fuel-bound nitrogen. As ϕ_{global} decreases (increasing staging), the nitrogen fraction shifts from unburned NH_3 toward oxidized species, primarily NO_x and N_2O. Pressure and heat loss effects further modify this redistribution, where elevated pressure in the present configuration increases convective heat losses, leading to higher NH_3 slip and promoting N_2O formation in the secondary stage. These trends allow direct visualization of how operating conditions govern nitrogen partitioning across the combustor.

Even under staged conditions ($\phi_{global} = 0.5$), these lingering emissions are still greater than the current regulatory limits for stationary gas turbines, which typically require NO_x emissions on the order of tens of ppm, often 9−25 ppm (15% dry O_2) depending on the turbine size and heat input.[32] In terms of staging air, decreasing ϕ_{global} shifts fuel nitrogen away from NH_3 slip and toward oxidized nitrogen species. For near-optimal primary conditions ($\phi_{primary} = 1.08$), both NO_x and N_2O remain below 0.5% of the fuel-nitrogen budget. In contrast, richer $\phi_{primary}$ operation at elevated pressures leads to a marked

https://doi.org/10.1021/acs.energyfuels.6c00593
Energy Fuels 2026, 40, 12098−12108

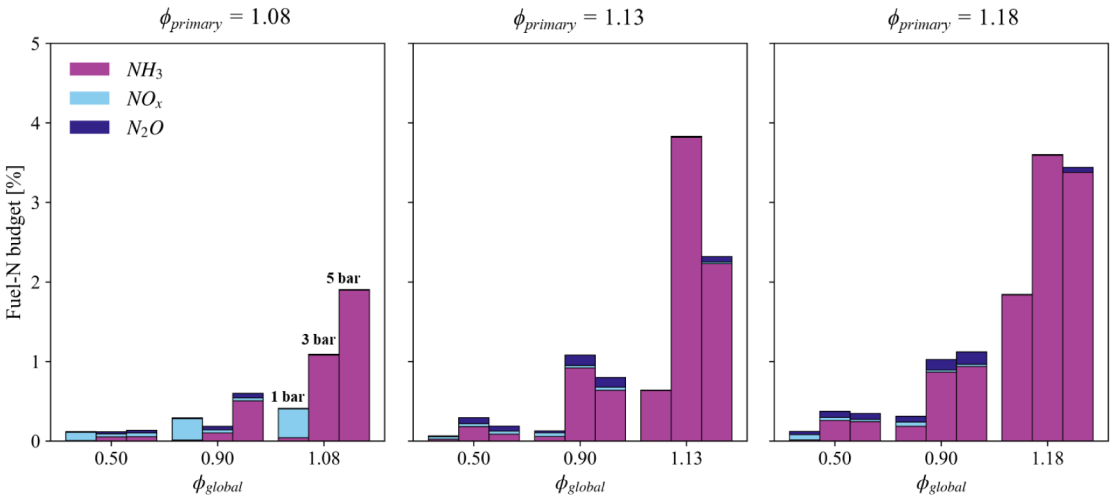

Figure 8. Exhaust emissions as a percentage of the fuel-bound nitrogen budget for the experimental test matrix. Note that the axis is truncated at 5% for readability. The three vertical bars at each ϕ_{global} value correspond to P_0 = 1, 3, and 5 bar, respectively.

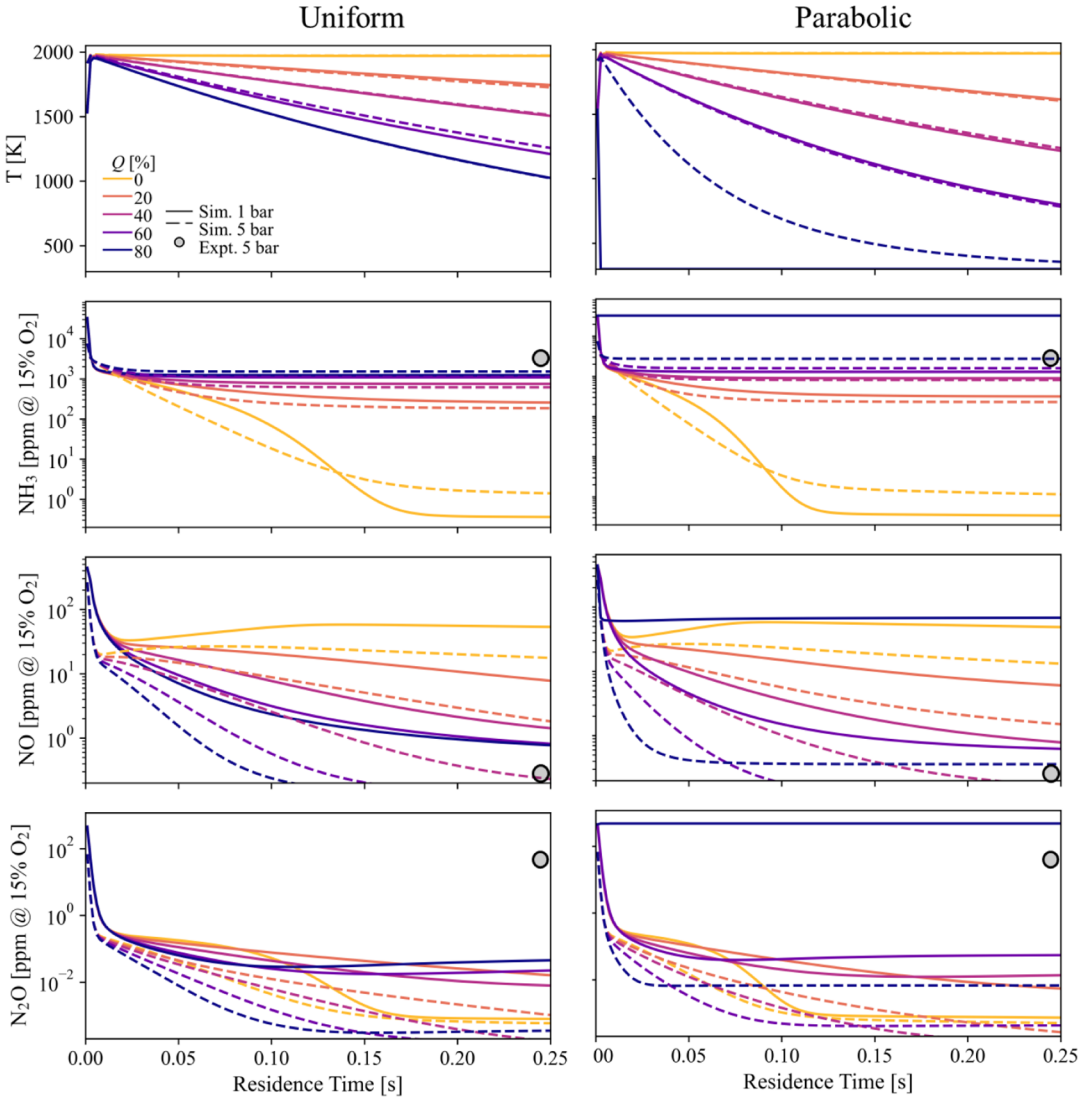

Figure 9. Uniform and parabolic CRN results for the Stagni mechanism overlaid with the experimental point at 250 ms, $\phi_{primary}$ of 1.18, and P_0 of 5 bar.

increase in the fraction of nitrogen existing as N_2O, particularly at high NH_3 slip conditions. The strong pressure sensitivity of the N_2O nitrogen fraction is consistent with the trends observed in Figure 7. It is attributed to enhanced heat losses at elevated pressures in the present

https://doi.org/10.1021/acs.energyfuels.6c00593
Energy Fuels 2026, 40, 12098−12108

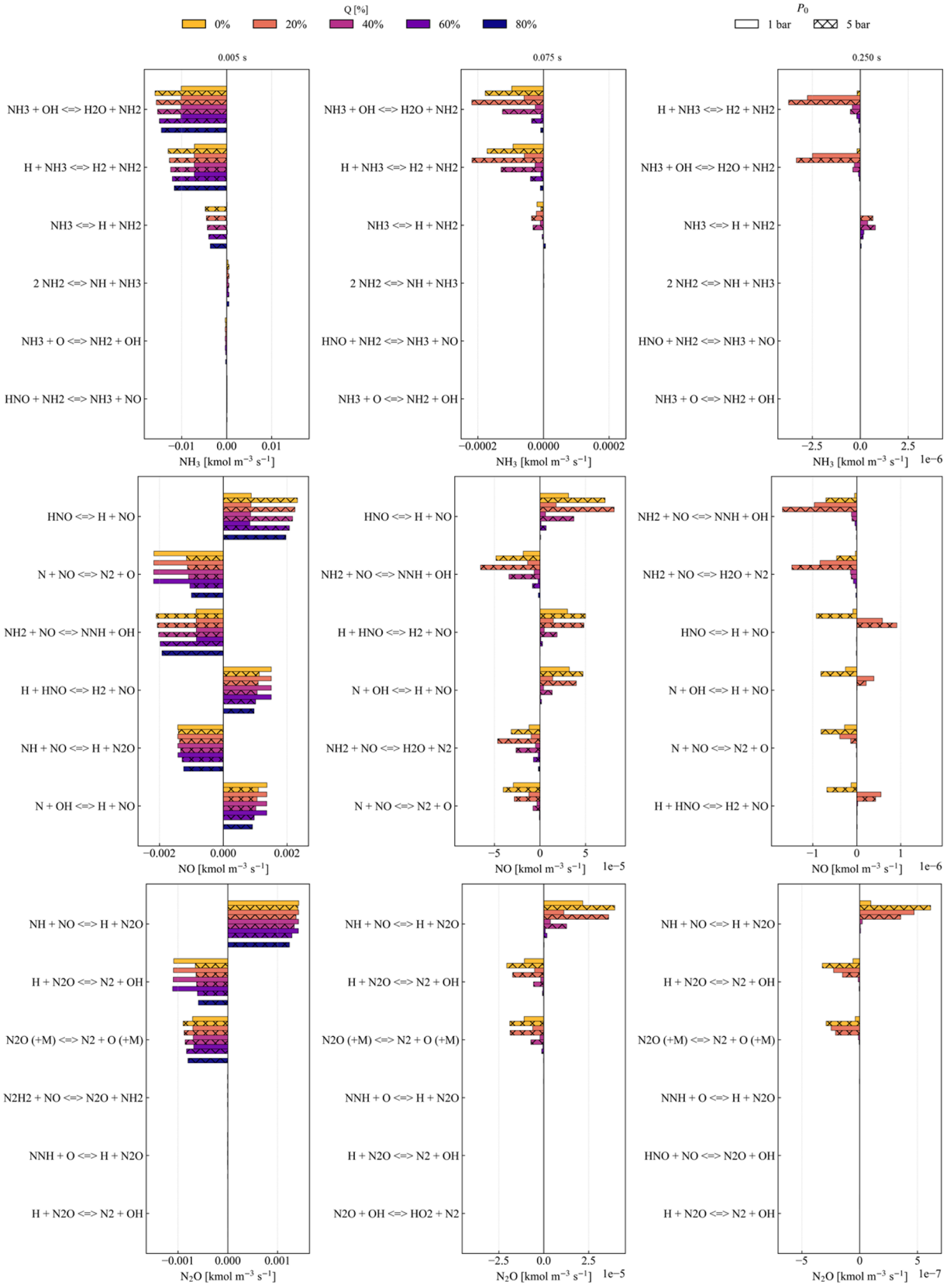

Figure 10. Uniform CRN ROP analysis for NH_3, NO, and N_2O at 5, 75, and 250 ms for $\phi_{primary}$ of 1.18 and P_0 of 5 bar using the Stagni mechanism.

experimental configuration. As pressure increases, shroud airflow rate increases, thereby increasing convective heat losses, which increase NH_3 slip into the secondary stage, where it is converted into N_2O due to rapid cooling from lean combustion.[33] Increased heat loss reduces postquench temperatures in the secondary stage, favoring reaction pathways that stabilize N_2O relative to NO_x or molecular nitrogen. This behavior highlights how nonoptimal combinations of residence time,

https://doi.org/10.1021/acs.energyfuels.6c00593
Energy Fuels 2026, 40, 12098−12108

pressure, and heat loss may redirect fuel-nitrogen toward N_2O formation.

CRN Results

The general emissions performance of the RRQL combustor diverges from both equilibrium and 1-D adiabatic computations. To better understand the underlying mechanisms driving these changes, the CRN shown in Figure 2 was run under the experimental conditions to examine the effects of heat losses and low-temperature regions in the combustor. The area-averaged parabolic and uniform CRNs are compared with overlaid experimental data in Figure 9, which shows results for $\phi_{primary}$ of 1.18 and P_0 at 1 and 5 bar using the Stagni mechanism.[27] The parabolic and tophat emissions did not differ significantly, as expected given the similarity in shape profiles shown in Figure 3. As such, the tophat emissions profile is included in the Supporting Information but is not shown separately here. Additionally, it should be noted that the CRN results presented in Figure 9 are mechanism-dependent. While the Zhang, Mei, and Stagni mechanisms showed similar general trends, the NH_3 sensitivity to P_0 and heat losses varied by up to 50%, as shown in the Supporting Information.

For the uniform CRN, as heat losses increase from 0% to 80% of the thermal power, the flame temperature drops from an adiabatic temperature of 1980 K to 1050 K at $\tau_{res,primary}$ of 250 ms. For reference, we estimate heat losses of approximately 45% during the 130 mm-long relaxation stage at 1 bar. These heat loss estimates are based on traversing thermocouple measurements along the combustor's centerline. The area-weighted parabolic CRN temperature, however, drops more significantly due to concentrated heat losses along the combustor, which, in turn, affects the emissions.

The decrease in temperature and heat losses significantly impacts computed exhaust emissions. For the uniform CRN at 5 bar, NH_3 levels rise from below 2 ppm (at 15% dry O_2) at 250 ms under adiabatic conditions to 1500 ppm (at 15% dry O_2) with 80% heat losses. Similarly, the computed NO_x emissions decrease by orders of magnitude as heat losses increase from 20% to 80%. This may be linked to increased NH_3 emissions under higher heat loss conditions, as NO_x production from fuel-bound nitrogen is derived from NH_3 cracking. Furthermore, NH_3 slip will continue to produce significant NO_x emissions in the secondary stage, and the level of NO_x emissions is expected to increase significantly. However, under adiabatic conditions in which all the fuel-bound nitrogen is released, NO_x emissions still drop to sub-20 ppm (15% dry O_2) from 500 ppm (15% dry O_2), showing NO_x relaxation as expected. P_0 monotonically influences NO_x emissions, with increased P_0 allowing relaxation toward lower equilibrium values. Finally, while the uniform CRN N_2O emissions are significantly affected by heat losses, all computed cases are sub-10 ppm (15% dry O_2) after 20 ms, indicating relatively low contributions.

For area-averaged parabolic CRN emissions, while the general trends remain unchanged, the magnitudes of unburned NH_3 and NO_x emissions are affected accordingly. For example, with 80% heat losses, the NH_3 emissions at 250 ms and 5 bar increase from 1500 ppm (15% O_2 dry) in the uniform case to 2500 (15% dry O_2 in the parabolic case. Furthermore, the NO_x emissions in the parabolic case with 80% heat losses only show relaxation until ~35 ms, after which most of the chemistry freezes due to high heat losses. This further highlights the importance of minimizing heat losses in systems with longer residence times to exploit rich NH_3 chemistry and NO_x relaxation. For lower heat loss conditions (20−60%), where NO_x relaxation does not freeze, NO_x emissions are lower in the parabolic case, which may be due to increased NH_3 slip. However, overall NO_x emissions will increase significantly in the secondary stage due to fuel-bound nitrogen from unburned NH_3 slip and shorter secondary stage residence times. Finally, N_2O emissions remain below 10 ppm (15% dry O_2), which is significantly lower than those of their experimental counterparts.

Additional rate of production (ROP) analysis is shown at selected $\tau_{res,primary}$ as shown in Figure 10 for the Stagni mechanism and the uniform CRN model. ROP plots for the Mei and Zhang mechanisms are located in the Supporting Information. With increasing $\tau_{res,primary}$ reaction rates transition from high-temperature chemistry to near-frozen chemical rates. At 5 ms, both NH_3 and NO chemistry are dominated by high-rate radical reactions, which exhibit large magnitudes and clear sensitivity to heat loss, though the overall pathway structure remains consistent across cases. However, at 75 ms, reaction rate magnitudes drop by roughly an order of magnitude, and the divergence between heat loss conditions becomes pronounced, indicating the onset of kinetic quenching. Key consumption pathways weaken significantly, especially under higher heat losses, where some NH_3 production occurs through NH_2 third-body reactions. At 250 ms, reaction rates are several orders of magnitude smaller, and only a few pathways persist with minimal activity, confirming that the chemistry has effectively frozen. Importantly, the dominant reactions remain largely the same across all conditions, but their magnitudes collapse dramatically with increasing heat loss, demonstrating that thermal losses largely suppress reaction rates rather than fundamentally altering the chemical pathways. This directly supports the interpretation that increased NH_3 slip and altered NO/N_2O partitioning arise from premature quenching of the relaxation stage chemistry, which is amplified under the nonuniform CRN distributions. Across all residence times, increasing pressure generally amplifies the magnitude of both production and consumption pathways, indicating enhanced reaction rates and more active radical-driven chemistry, although the dominant reaction pathways themselves remain largely unchanged.

Figure 11 illustrates the nitrogen budget for both the parabolic and uniform CRNs with experimental data at $\phi_{primary} = \phi_{global}$ of

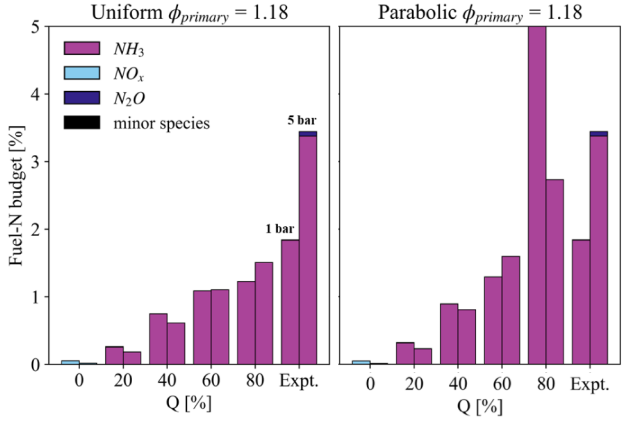

Figure 11. Exhaust emissions at 250 ms as a percentage of the fuel-bound nitrogen budget for the parabolic and uniform CRNs using the Stagni mechanism with experimental results. Note that the axis is truncated at 5% for readability. The two vertical bars at each ϕ_{global} value correspond to P_0 = 1 and 5 bar, respectively.

https://doi.org/10.1021/acs.energyfuels.6c00593
Energy Fuels 2026, 40, 12098−12108

1.18, P_0 at 1 and 5 bar, and 250 ms. Similarly to the previous section, emissions are expressed as a percentage of the fuel-bound nitrogen inventory, with the top four contributing species being NH_3, NO (reported as total NO_x or the sum of NO and NO_2 in Figure 11), NH_2, and N_2O. Note that NH_2 is not reported in Figure 11 because it is not a major pollutant, and its concentrations are on the order of parts-per-billion. The nitrogen budget representation allows direct visualization of how heat loss magnitude and distribution shift nitrogen partitioning among NH_3, NO_x, and N_2O. Increasing heat loss suppresses NH_3 cracking in the relaxation stage, results in greater NH_3 carryover, and reduces NO_x formation, with implications for downstream emissions in the secondary stage. Across all conditions examined, only a small fraction of the fuel-bound nitrogen exits the relaxation stage as NO_x or N_2O and no more than 4% of the fuel-bound nitrogen is NH_3 slip at these conditions, except for the parabolic 1 bar 80% heat loss case, which shows large quantities of NH_3 due to a lack of ignition.

The uniform CRN shows that NH_3 levels increase from ∼0.1% under adiabatic conditions to ∼1.5% with 80% heat losses. At 60% heat losses, the 5-bar case produces more NH_3, showing the nonmonotonicity of NH_3 with pressure under high heat losses. The parabolic CRN also shows this trend, except for the 1-bar 80% heat loss case, which shows large quantities of NH_3 due to a lack of ignition. Additionally, the NH_3 levels increase rapidly, from ∼0.1% under adiabatic conditions to ∼4% with 80% heat losses at 5 bar, demonstrating the effects of near-wall cooling. Taken together, these results indicate that increasing pressure, in combination with elevated heat losses, suppresses nonoxidative NH_3 cracking during the relaxation stage, leading to greater NH_3 carryover and, consequently, enhanced fuel-NO_x and N_2O formation in the secondary stage. This pressure-induced reduction in NH_3 decomposition is consistent with theoretical predictions showing diminished NH_3 cracking efficiency at higher pressures.[34,35]

Comparison with Experimental Data

The experimental data at 5 bar and $\tau_{res,primary}$ of 250 ms is also shown in Figure 9. It most closely resembles the 80% heat losses for the uniform and parabolic CRNs. For NH_3 emissions, as heat losses increase, the trend of decreasing NH_3 emissions with increasing P_0 reverses, so that NH_3 emissions increase with P_0. This phenomenon is present in the experimental data shown in Figure 6, which indicates experimental heat losses exceeding 40%. The experimental NO_x emissions closely match the 40−60% heat loss case, although the emissions measurements are near the instrument's detection limit, as noted in Figure 5.

The N_2O emissions most closely match the 80% heat loss case; however, they are orders of magnitude higher than those in the simulations. Notably, in Figure 11, the CRNs underpredict the redistribution of fuel-bound nitrogen to NH_3 and N_2O, even under high-heat loss conditions. High N_2O emissions are a strong indicator of elevated heat losses from the combustor walls. Still, this deviation may also reflect the need to improve the underlying kinetic mechanisms to achieve a higher-fidelity treatment of loss profiles.

Previous emissions data taken in this combustor at 1 bar with a single-point probe at various radial and axial positions show that, at 80 ms from the flame brush, NH_3 emissions may increase from 30% to 300% from the centerline to the wall, while NO_x and N_2O both vary by less than 15%.[15] This suggests that the strong NH_3 response to increased P_0 and shroud cooling is unlikely to be uniform across the radius and may be amplified in a near-wall region. However, the variability from 30% to 300% demonstrates that this is highly dependent on flame shape and operating conditions. The comparison of the experimental data with the CRN, shown in Figure 9, requires NH_3 levels to experience an effective temperature drop of several hundred Kelvin, corresponding to 40−80% heat losses, considering the more realistic parabolic profile in the regions that dominate the NH_3 slip. The entire cross-section of the combustor may be quenched, but a strongly cooled near-wall flow can also supply a disproportionate amount of NH_3 to the rake probe. Further experimental measurements of core and wall emissions are required to better understand these effects.

CONCLUSIONS

An experimental study was conducted to examine the impact of pressure on an RRQL combustor. Kinetic modeling aligns with experimental trends, unlike previous adiabatic 1-D and equilibrium calculations, and the modeling indicates high heat losses in the system. The main conclusions are as follows:

- Out of the initial fuel-bound nitrogen, experimentally, less than 4% is partitioned among minor nitrogen species, including NH_3, NO_x, and N_2O. NH_3 slip and N_2O are prominent for richer $\phi_{primary}$ and elevated heat loss conditions. Chemical reactor network modeling underpredicts the NH_3 and N_2O emissions, even under high heat loss conditions, when compared with the experimental data.
- NH_3 emissions increased significantly with pressure, consistent with reduced postflame temperatures. Heat losses of 60−80% of the thermal power at primary residence times of 250 ms were inferred from comparisons with predictions from chemical reactor network modeling. Further work is needed to understand whether high levels of NH_3 slip are dominated by near-wall quenching or low core temperatures.
- NO_x relaxation was documented to reach near-equilibrium levels within ∼250 ms, even at high heat loss conditions, with up to 98% of NO_x production occurring in the secondary stage.
- N_2O emissions increased substantially under staged conditions, reaching 20−40% of total NO_x−N_2O emissions, which is underpredicted by chemical reactor network modeling.
- While the Mei, Zhang, and Stagni mechanisms predicted similar qualitative trends, NH_3 sensitivity to pressure and heat losses differed by up to 50%, underscoring the need to continue validating the NH_3 kinetics.

This work shows that higher heat losses lead to lower nonoxidative NH_3 cracking in the relaxation stage, driving more fuel-NO_x and N_2O in the secondary stage. However, overall emissions from the full RRQL architecture at 5 bar were low, with ∼70 ppm of NO_x, 30 ppm of NH_3, and 15 ppm of N_2O (all corrected to 15% O_2) even under nonoptimal heat loss conditions, demonstrating the potential for low-NO_x NH_3 combustion with the RRQL architecture.

ASSOCIATED CONTENT

Supporting Information

The Supporting Information is available free of charge at https://pubs.acs.org/doi/10.1021/acs.energyfuels.6c00593.

- Tophat CRN results using the Stagni mechanism overlaid with the experimental point at 250 ms, $\phi_{primary}$ of 1.18, and P_0 of 5 bar; uniform CRN results overlaid with the experimental point at 250 ms, $\phi_{primary}$ of 1.18, and P_0 of 5 bar for the Stagni, Mei, and Zhang mechanisms; uniform CRN ROP analysis for NH_3, NO, and N_2O at 5, 75, and 250 ms for $\phi_{primary}$ of 1.18 and P_0 of 5 bar using the Mei mechanism; and uniform CRN ROP analysis for NH_3,

https://doi.org/10.1021/acs.energyfuels.6c00593
Energy Fuels 2026, 40, 12098−12108

NO, and N_2O at 5, 75, and 250 ms for $\phi_{primary}$ of 1.18 and P_0 of 5 bar using the Zhang mechanism (PDF)

AUTHOR INFORMATION

Corresponding Author

Renee Cole − *Ben T. Zinn Combustion Laboratory, Georgia Institute of Technology, Atlanta, Georgia 30332, United States*; orcid.org/0009-0003-8115-764X; Email: rcole36@gatech.edu

Authors

Ananth S. Nayak − *Ben T. Zinn Combustion Laboratory, Georgia Institute of Technology, Atlanta, Georgia 30332, United States*

Cristian Avila − *Universidad de Antioquia, Medellín, Antioquia 050034, Colombia*; orcid.org/0000-0002-8396-6163

David R. Noble − *Electric Power Research Institute (EPRI), Charlotte, North Carolina 28262, United States*

David Wu − *Electric Power Research Institute (EPRI), Charlotte, North Carolina 28262, United States*

Benjamin Emerson − *Ben T. Zinn Combustion Laboratory, Georgia Institute of Technology, Atlanta, Georgia 30332, United States*

Timothy Lieuwen − *Ben T. Zinn Combustion Laboratory, Georgia Institute of Technology, Atlanta, Georgia 30332, United States*

Complete contact information is available at: https://pubs.acs.org/10.1021/acs.energyfuels.6c00593

Author Contributions

The manuscript was written through the contributions of all authors. All authors have given approval to the final version of the manuscript.

Funding

This work was performed in part under funding from the Georgia Institute of Technology, DOE/National Energy Technology Laboratory (DE-FE0032079), and the EPRI-GTI Energy Low Carbon Resources Initiative (LCRI).

Notes

The authors declare no competing financial interest.

ACKNOWLEDGMENTS

This work was performed in part under funding from DOE/National Energy Technology Laboratory (Grant DE-FE0032079) and from the EPRI-GTI Energy Low Carbon Resources Initiative (LCRI). The authors gratefully acknowledge the technical contributions and insights of Mark Winquist and John Vega at GTI-Energy.

ABBREVIATIONS

A_{total}, total cross-sectional area; A_j, cross sectional-area of radial subregion; a, parabolic shape parameter; b, tophat shape parameter; CRN, chemical reactor network; δ, thickness of near-wall annulus; H_2, hydrogen; η, nondimensional radial coordinate; η_c, nondimensional cutoff radius for tophat; NH_3, ammonia; NO_x, nitric oxides; N_2O, nitrous oxide; N_b, number of radial bins; P_0, inlet pressure; PFR, plug flow reactor; PFR_j, radial plug flow reactor; PSR, perfectly stirred reactor; Q, thermal power; Q_{PFR}, plug flow reactor heat loss; r, radial position; R, combustor liner radius; ROP, Rate of Production; RQL, Rich-Quench-Lean;; RRQL, Rich-Relax-Quench-Lean; S_g, swirl number; T_0, inlet temperature; Ts, inlet shroud temperature; $\tau_{res,primary}$, primary stage residence time; U_0, nozzle bulk velocity; w, area-weighted average; X_{NH3}, ammonia mole fraction; $\overline{\psi}$, area-weighted average state;; ψ_j, radial state; $\phi_{primary}$, primary equivalence ratio; ϕ_{global}, global equivalence ratio

REFERENCES

(1) Elbaz, A. M.; Wang, S.; Guiberti, T. F.; Roberts, W. L. Review on the recent advances on ammonia combustion from the fundamentals to the applications. *Fuel Commun.* **2022**, *10*, 100053.

(2) Valera-Medina, A.; Xiao, H.; Owen-Jones, M.; David, W. I. F.; Bowen, P. J. Ammonia for power. *Prog. Energy Combust. Sci.* **2018**, *69*, 63−102.

(3) Hayakawa, A.; Goto, T.; Mimoto, R.; Arakawa, Y.; Kudo, T.; Kobayashi, H. Laminar burning velocity and Markstein length of ammonia/air premixed flames at various pressures. *Fuel* **2015**, *159*, 98−106.

(4) Pfahl, U. J.; Ross, M. C.; Shepherd, J. E.; Pasamehmetoglu, K. O.; Unal, C. Flammability limits, ignition energy, and flame speeds in H2−CH4−NH3−N2O−O2−N2 mixtures. *Combust. Flame.* **2000**, *123* (1), 140−158.

(5) Hayakawa, A.; Goto, T.; Mimoto, R.; Kudo, T.; Kobayashi, H. NO formation/reduction mechanisms of ammonia/air premixed flames at various equivalence ratios and pressures. *Mech. Eng. J.* **2015**, *2* (1), 14−00402.

(6) Zhu, X.; Khateeb, A. A.; Guiberti, T. F.; Roberts, W. L. NO and OH* emission characteristics of very-lean to stoichiometric ammonia−hydrogen−air swirl flames. *Proc. Combust. Inst.* **2021**, *38* (4), 5155−5162.

(7) Khateeb, A. A.; Guiberti, T. F.; Wang, G.; Boyette, W. R.; Younes, M.; Jamal, A.; Roberts, W. L. Stability limits and NO emissions of premixed swirl ammonia-air flames enriched with hydrogen or methane at elevated pressures. *Int. J. Hydrogen Energy* **2021**, *46* (21), 11969−11981.

(8) Zhang, M.; Wei, X.; An, Z.; Okafor, E. C.; Guiberti, T. F.; Wang, J.; Huang, Z. Flame stabilization and emission characteristics of ammonia combustion in lab-scale gas turbine combustors: Recent progress and prospects. *Prog. Energy Combust. Sci.* **2025**, *106*, 101193.

(9) Agustin, V. M.; Syed, M.; Daniel, P.; Phil, B. Ammonia. In *Renewable Fuels: sources, Conversion, and Utilization*, O'Connor, J.; Noble, B.; Lieuwen, T., Eds.; Cambridge University Press: Cambridge, United Kingdom, 2022; pp. 245−274.

(10) Rocha, R. C.; Costa, M.; Bai, X.-S. Combustion and Emission Characteristics of Ammonia under Conditions Relevant to Modern Gas Turbines. *Combust. Sci. Technol.* **2021**, *193* (14), 2514−2533.

(11) Lieuwen, T. C.; Yang, A. U. *Vigor, Gas Turbine Emissions*; Cambridge University Press: "CY -Cambridge, UK", 2013.

(12) Guteša Božo, M.; Mashruk, S.; Zitouni, S.; Valera-Medina, A. Humidified ammonia/hydrogen RQL combustion in a trigeneration gas turbine cycle. *Energy Convers. Manage.* **2021**, *227*, 113625.

(13) Okafor, E. C.; Somarathne, K. D. K. A.; Hayakawa, A.; Kudo, T.; Kurata, O.; Iki, N.; Kobayashi, H. Towards the development of an efficient low-NOx ammonia combustor for a micro gas turbine. *Proc. Combust. Inst.* **2019**, *37* (4), 4597−4606.

(14) Somarathne, K. D. K. A.; Yamashita, H.; Colson, S.; Oku, K.; Honda, K.; Okafor, E. C.; Hayakawa, A.; Kudo, T.; Kobayashi, H. Towards the development of liquid ammonia/air spray combustion in a gas turbine-like combustor at moderately high pressure. *Appl. Energy Combust. Sci.* **2023**, *16*, 100215.

(15) Cole, R.; Avila Jimenez, C. D.; Noble, D. R.; Steele, R.; Wu, D.; Emerson, B.; Lieuwen, T. Toward the Development of an RRQL System—Part I: Swirl Pattern Effect on Exhaust Emissions and Chemiluminescence Distribution for NH3−Air Premixed Swirl Flames. *J. Eng. Gas Turbines Power.* **2025**, *148* (7), 071001.

(16) Avila Jimenez, C. D.; Cole, R.; Noble, D. R.; Steele, R.; Wu, D.; Emerson, B.; Lieuwen, T. Toward the Development of an NH3-RRQL System—Part II: Effects of the Primary Combustion Zone Length and

Secondary Stage Number of Holes on Stability and Emissions. *J. Eng. Gas Turbines Power.* **2025**, *148* (7), 071002.
(17) Gubbi, S.; Cole, R.; Emerson, B.; Noble, D.; Steele, R.; Sun, W.; Lieuwen, T. Air Quality Implications of Using Ammonia as a Renewable Fuel: How Low Can NOx Emissions Go? *ACS Energy Lett.* **2023**, *8* (10), 4421−4426.
(18) Rana, S.; Papas, P.; Smith, L. L.; Sung, C.-J. Reducing NOx Emissions in Ammonia Combustors. *J. Eng. Gas Turbines Power.* **2025**, *148*, 011015.
(19) Gubbi, S.; Cole, R.; Emerson, B.; Noble, D.; Steele, R.; Sun, W.; Lieuwen, T. Evaluation of Minimum NOx Emission From Ammonia Combustion. *J. Eng. Gas Turbines Power.* **2024**, *146* (3), 031023.
(20) Chen, Y.-R.; Reibel, G.; Oku, K.; Yamashita, H.; Hayakawa, A.; Kudo, T.; Ito, H.; Somarathne, K. D. K. A.; Kobayashi, H. Effects of wall heat loss on emission characteristics of liquid ammonia spray combustion using a swirling burner. *Appl. Energy Combust. Sci.* **2025**, *23*, 100370.
(21) Okafor, E. C.; Tsukamoto, M.; Hayakawa, A.; Somarathne, K. D. K. A.; Kudo, T.; Tsujimura, T.; Kobayashi, H. Influence of wall heat loss on the emission characteristics of premixed ammonia-air swirling flames interacting with the combustor wall. *Proc. Combust. Inst.* **2021**, *38* (4), 5139−5146.
(22) Zhang, M.; Xu, W.; Wang, R.; Wei, X.; Wang, J.; Huang, Z.; Tan, H. Wall heat loss effect on the emission characteristics of ammonia swirling flames in a model gas turbine combustor. *Combust. Flame* **2023**, *256*, 112955.
(23) Bedick, C.; Boyette, W. Chemical Reactor Network Modeling of Ammonia Rich-Quench-Lean Combustion Using a Partially Stirred Reactor Approach. In *Turbo Expo*; ASME, 2025, Vol.*88780*, pp.V03AT04A053.
(24) Avila Jimenez, C. D.; Cole, R.; Parnell, J.; Peckham, M.; Wu, D.; Emerson, B. Exhaust emissions point measurements on the secondary stage of an NH3-RRQL system. *Proc. Combust. Inst.* **2025**, *41*, 105791.
(25) Cole, R.; Gubbi, S.; Wu, D.; Emerson, B.; Noble, D. R.; Steele, R.; Sun, W.; Lieuwen, T. Rich Ammonia Flame Shapes and No Relaxation: Facility Development and Characterization.In *Turbo Expo: Power for Land, Sea, and Air*; ASME, 2024,Vol. *87943*, V03AT04A012.
(26) Baukal, C. E.; Eleazer, P. B. Quantifying NOx for Industrial Combustion Processes. *J. Air Waste Manage. Assoc.* **1998**, *48* (1), 52−58.
(27) Stagni, A.; Arunthanayothin, S.; Dehue, M.; Herbinet, O.; Battin-Leclerc, F.; Bréquigny, P.; Mounaïm-Rousselle, C.; Faravelli, T. Low- and intermediate-temperature ammonia/hydrogen oxidation in a flow reactor: Experiments and a wide-range kinetic modeling. *Chem. Eng. J.* **2023**, *471*, 144577.
(28) Mei, B.; Zhang, X.; Ma, S.; Cui, M.; Guo, H.; Cao, Z.; Li, Y. Experimental and kinetic modeling investigation on the laminar flame propagation of ammonia under oxygen enrichment and elevated pressure conditions. *Combust. Flame* **2019**, *210*, 236−246.
(29) Zhang, X.; Moosakutty, S. P.; Rajan, R. P.; Younes, M.; Sarathy, S. M. Combustion chemistry of ammonia/hydrogen mixtures: Jet-stirred reactor measurements and comprehensive kinetic modeling. *Combust. Flame* **2021**, *234*, 111653.
(30) Chterev, I.; Foley, C. W.; Foti, D.; Kostka, S.; Caswell, A. W.; Jiang, N.; Lynch, A.; Noble, D. R.; Menon, S.; Seitzman, J. M.; Lieuwen, T. C. Flame and Flow Topologies in an Annular Swirling Flow. *Combust. Sci. Technol.* **2014**, *186* (8), 1041−1074.
(31) Greenhouse Gas Protocol Global Warming Potential Values. *World Resources Institute*; Greenhouse Gas Protocol, 2016.
(32) Agency, U. S. E. P. *New Source Performance Standards for Stationary Combustion Turbines.*; U.S. Environmental Protection Agency: Washington, DC, 2024.
(33) Avila, C.; Wang, G.; Zhu, X.; Es-Sebbar, E.-T.; Abdullah, M.; Younes, M.; Jamal, A.; Guiberti, T.; Roberts, W. L. Lean Stability Limits and Exhaust Emissions of Ammonia-Methane-Air Swirl Flames at Micro Gas Turbine Relevant Pressure. In *Turbo Expo: Power for Land, Sea, and Air*; ASME, 2022, Vol.*85994*, pp.V03AT04A004.
(34) Shafie, P.; De Champlain, A.; Lepine, J. Theoretical investigation of hydrogen-rich fuel production through ammonia decomposition. *Open Chem.* **2024**, *22* (1), 20240020.
(35) Spatolisano, E.; Pellegrini, L. A.; de Angelis, A. R.; Cattaneo, S.; Roccaro, E. Ammonia as a Carbon-Free Energy Carrier: NH3 Cracking to H2. *Ind. Eng. Chem. Res.* **2023**, *62* (28), 10813−10827.

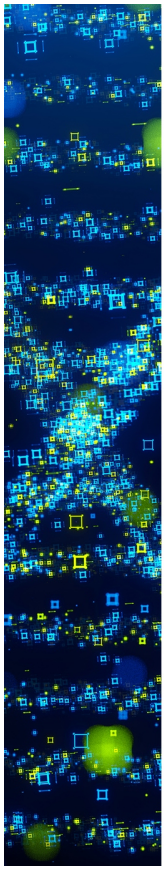

https://doi.org/10.1021/acs.energyfuels.6c00593
Energy Fuels 2026, 40, 12098−12108